

1 **Using different assumptions of aerosol mixing state and chemical**
2 **composition to predict CCN concentrations based on field**
3 **measurements in urban Beijing**

4 **Jingye Ren¹, Fang Zhang^{1,2*}, Yuying Wang¹, Don Collins³, Xinxin Fan¹, Xiaoai**
5 **Jin¹, Weiqi Xu^{3,4}, Yele Sun^{3,4}, Maureen Cribb⁵, Zhanqing Li^{1,5}**

6
7 *¹College of Global Change and Earth System Science, Beijing Normal University,*
8 *Beijing 100875, China*

9 *²Joint Center for Global Change Studies (JCGCS), Beijing 100875, China*

10 *³Department of Atmospheric Sciences, Texas A&M University, College Station, TX,*
11 *USA*

12 *⁴State Key Laboratory of Atmospheric Boundary Layer Physics and Atmospheric*
13 *Chemistry, Institute of Atmospheric Physics, Chinese Academy of Sciences, Beijing*
14 *100029, China*

15 *⁵University of Chinese Academy of Sciences, Beijing 100049, China*

16 *⁶Earth System Science Interdisciplinary Center and Department of Atmospheric and*
17 *Oceanic Science, University of Maryland, College Park, Maryland, USA*

18
19
20
21
22 ***Correspondence to: Fang Zhang (fang.zhang@bnu.edu.cn)**

25 **Abstract**

26 Understanding the impacts of aerosol chemical composition and mixing state on
27 cloud condensation nuclei (CCN) activity in polluted areas is crucial for accurately
28 predicting the CCN number concentrations (N_{CCN}). In this study, we predict N_{CCN}
29 under five assumed schemes of aerosol chemical composition and mixing state based
30 on field measurements in Beijing during the winter of 2016. Our results show that the
31 best closure is achieved with an assumption of a size dependent chemical composition
32 for which sulfate, nitrate, secondary organic aerosols and aged black carbon are
33 internally mixed with each other but externally mixed with primary organic aerosol
34 and fresh black carbon (external-internal size-resolved, abbreviated as EI-SR scheme).
35 The resulting ratios of predicted-to-measured N_{CCN} ($R_{CCN_p/m}$) were 0.90–0.98 under
36 both clean and polluted conditions. Assumption of an internal mixture and bulk
37 chemical composition (INT-BK scheme) shows good closure with $R_{CCN_p/m}$ of
38 1.01–1.16 under clean conditions, implying that it is adequate for CCN prediction in
39 continental clean regions. On polluted days, assuming the aerosol is internally mixed
40 and has a chemical composition that is size dependent (INT-SR scheme) achieves
41 better closure than the INT-BK scheme due to the heterogeneity and variations in
42 particle composition at different sizes. The improved closure achieved using the
43 EI-SR and INT-SR assumptions highlight the importance of measuring size-resolved
44 chemical composition for CCN predictions in polluted regions. N_{CCN} is significantly
45 underestimated (with $R_{CCN_p/m}$ of 0.66–0.75) when using the schemes of external
46 mixtures with bulk (EXT-BK scheme) or size-resolved composition (EXT-SR

47 scheme), implying that primary particles experience rapid aging and physical mixing
48 processes in urban Beijing. However, our results show that the aerosol mixing state
49 plays a minor role in CCN prediction when the κ_{org} exceeds 0.1.

50 **1 Introduction**

51 Atmospheric aerosol particles can serve as cloud condensation nuclei (CCN) and,
52 in turn, affect the optical and microphysical properties of clouds (Twomey, 1977;
53 Albrecht, 1989; Charlson et al., 1992). Additionally, an increase in the aerosol number
54 concentration may suppress precipitation in shallow clouds and promote it in deep
55 convective clouds (Rosenfeld et al., 2008; Li et al., 2011). A key challenge to
56 understanding indirect aerosol effects is quantifying CCN spectra and their spatial and
57 temporal variations.

58 The ability of particles to act as CCN mainly depends on their size, chemical
59 composition, and mixing state (McFiggans et al., 2006; Dusek et al., 2006; Ma et al.,
60 2013). The impacts of the size distribution and chemical composition on CCN activity
61 has been discussed in previous studies (Dusek et al., 2006, Ervens et al., 2007;
62 Broekhuizen et al., 2006; Yum et al., 2005, 2007; Wiedensohler et al., 2009; Deng et
63 al., 2013; Zhang et al., 2014, 2016; Kawana et al., 2016). The effect of chemical
64 composition can be represented by a hygroscopicity parameter (κ) (Petters and
65 Kreidenweis, 2007) that is often used to predict N_{CCN} (Moore et al., 2012; Zhang et al.,
66 2014). However, particle composition may vary from single species to a mixture of
67 multiple species for a given size. A description of size-resolved chemical composition

68 thus leads to a better prediction of N_{CCN} because it allows variation of κ with size
69 (Medina et al., 2007; Wang et al., 2010; Meng et al., 2014). Variations in mixing state
70 also impact N_{CCN} prediction, with the effect dependent on the hygroscopicity of the
71 organic component (Wang et al., 2010). The assumption of internal mixtures has been
72 demonstrated to predict N_{CCN} well (Ervens et al., 2007; Chang et al., 2007; Andreae
73 and Rosenfeld, 2008; Gunthe et al., 2009; Rose et al., 2008; Meng et al., 2014; Zhang
74 et al., 2014; Li et al., 2017). However, some studies have shown that detailed
75 information about the chemical composition and the mixing state is required because
76 of the complexity of the hygroscopicity of organics (Broekhuizen et al., 2006; Bhattu
77 and Tripathi, 2015) and the differences in the CCN activity between fresh and aged
78 aerosols (Gunthe et al., 2011). Therefore, the impact of different assumptions
79 concerning the mixing state and chemical composition on accurately quantifying CCN
80 concentrations needs further investigation, especially in heavily polluted regions.

81 Beijing, a typical polluted city, frequently experiences severe haze pollution
82 episodes (Sun et al., 2013; Guo et al., 2014; Zheng et al., 2015), particularly in winter.
83 Several recent studies have focused on studying particle hygroscopicity (Wu et al.,
84 2016; Wang et al., 2017) and chemical composition (Gunthe et al., 2011), and using
85 bulk κ to predict CCN in Beijing (e.g., Liu et al., 2014; Zhang et al., 2017). However,
86 to our knowledge, a comprehensive CCN closure test considering chemical
87 composition and mixing state is lacking for this polluted urban area. In particular, the
88 transformation of the particle mixing state may be very quick during severe pollution
89 conditions (Wu et al., 2016). During pollution events, the hygroscopicity of organics

90 and the CCN activity are often enhanced rapidly with the aging process (Gunthe et al.,
91 2011; Kawana et al., 2016). Therefore, the characterization and parameterization of
92 CCN activation may be more challenging in polluted regions due to the impacts of
93 organics (Wang et al., 2010; Meng et al., 2014; Che et al., 2016; Zhang et al., 2016).

94 In this study, we use size-resolved measurements of CCN activity and
95 size-resolved chemical composition information to predict N_{CCN} using field
96 measurement data collected in Beijing during the winter of 2016. The CCN closure
97 study is carried out using five schemes with different assumptions of particle mixing
98 state and chemical composition. By classifying the data into three different periods
99 (nighttime, noontime, and the evening rush hour), we also investigate the variations in
100 aerosol mixing state from fresh to relatively aged aerosols. The sensitivity of
101 predicted N_{CCN} to the particle mixing state and organic volume fraction with the aging
102 of organic particles is also presented in the last section of the study.

103 **2 Measurements and data**

104 Data used here were measured from 15 November to 14 December 2016
105 during the Air Pollution and Human Health (APHH) field campaign at the Institute of
106 Atmospheric Physics (IAP), Chinese Academy of Sciences (39.97°N, 116.37°E),
107 which is a typical urban site with influences from traffic and cooking emissions (Sun
108 et al., 2015). The sampling instruments were placed in a container at ground level.

109 The particle number size distribution (PNSD) was measured by a Scanning

110 Mobility Particle Sizer (SMPS; [Wang et al., 2003](#)). The SMPS consists of a
111 differential mobility analyzer (DMA; model 3081, TSI Inc.) and a condensation
112 particle counter (CPC; model 3772, TSI Inc.). Measurements of size-resolved CCN
113 efficiency spectra were made by an integrated system combining the SMPS ([Wang et
114 al., 2003](#)) and a Droplet Measurement Technologies CCN counter (DMT-CCNc;
115 [Lance et al., 2006](#)). The procedure to couple the SMPS and the DMT-CCNc
116 developed by [Moore et al. \(2010\)](#) was followed. Atmospheric particles were sampled
117 from an inlet located 1.5 m above the roof of the container and were then passed
118 through a silica gel desiccant drying tube and into the SMPS. The relative humidity
119 of the sample flow was below 30%. The sample flow exiting the DMA was divided
120 into 0.5 lpm for the CCNc and 0.5 lpm for the CPC. Before and after the field
121 campaign ammonium sulfate was used to calibrate the supersaturation (SS) levels of
122 the CCNc with longitudinal temperature differences of 2, 3, 5, 8, 10, 13, and 15 K as
123 shown in Fig. S1. Based on this calibration, the five effective SS levels were 0.12,
124 0.14, 0.23, 0.40, and 0.76%.

125 The PNSD spanned the size range of 10–550 nm with a measurement scan time
126 of 5 min. Total particle or condensation nuclei (CN) size distributions were calculated
127 with the multiple charge correction and transfer function used in the TSI-AIM
128 software. The CN number concentration (N_{CN}) is the total aerosol number
129 concentration and is obtained by integrating the PNSD over the size range of 10–550
130 nm. The full measurement cycle of the CCNc for the five SS levels took one hour (20
131 min for 0.12% and 10 min for each higher SS). Size-resolved CCN efficiency data

132 were inverted with a multiple charge correction (Moore et al., 2010). The CCN
133 number size distribution was calculated by multiplying the CCN efficiency spectrum
134 by the particle number size distribution. The total CCN concentration was then
135 calculated by integrating the size-resolved N_{CCN} . The bulk activation ratio (AR) was
136 calculated as N_{CCN}/N_{CN} . The results were stratified between polluted and background
137 conditions with an assumed threshold PM1 mass concentration of $50 \mu\text{g m}^{-3}$.

138 An Aerodyne High-Resolution Time-of-Flight Aerosol Mass Spectrometer
139 (HR-ToF-AMS; DeCarlo et al., 2006) was housed in a sampling room on the rooftop
140 of a two-story building to measure size-resolved non-refractory submicron aerosols,
141 including organics, sulfate, nitrate, ammonium, and chloride with a time resolution of
142 ~ 5 min. More details about the HR-ToF-AMS and the measurement site have been
143 described in previous studies (Sun et al., 2010; Sun et al., 2016). The organics are
144 classified by using Positive Matrix Factorization (PMF) (Paatero and Tapper, 1994) ,
145 considering as being composed of two components: primary organic aerosol (POA)
146 representing non-hygroscopic particles and secondary organic aerosol (SOA)
147 representing hygroscopic particles. The first component consists mainly of
148 hydrocarbon-like organic aerosol (HOA), a surrogate of primary organic aerosol
149 (POA) from local combustion sources. And the size distribution of the primary OA
150 was measured by the estimated size-distribution of the C_4H_9^+ fragment (Aiken et al.,
151 2009; Zhang et al., 2005). The size distribution of the SOA was calculated as the
152 difference between the total OA and POA.

153 The black carbon (BC) mass concentration was measured using a
154 seven-wavelength aethalometer (AE33, Magee Scientific Corp.). [Zhao et al. \(2017\)](#)
155 provides details about this instrument and the measurements it makes. Due to an
156 absence of size-resolved BC measurements, the BC size distribution was calculated
157 from the combination of an approximately lognormal distribution measured by a
158 single particle soot photometer (SP2, DMT) ([Wu et al., 2017](#)) and the total BC mass
159 concentration. Note that because the SP2 measures BC core diameter instead of the
160 diameter of the BC-containing particle, it would overestimate the BC mass
161 concentration of smaller particles but underestimate that of the larger ones. Such
162 overestimation would likely lead to an underestimation of N_{CCN} due to the increased
163 mass fraction of BC of total particles. The uncertainty of this effect is evaluated in
164 Section 4.3. The fresh and aged BC size distributions are determined from the total
165 BC size distribution measured by the SP2 ([Wu et al., 2017](#)) and from the dependence
166 of the fraction of internally mixed soot (F_{in}) on particle diameter (D_p) observed in
167 urban Beijing by [Cheng et al. \(2012\)](#). The instruments produce different diameters. In
168 this paper, we have unified both the aerodynamic diameter from AMS and volume
169 equivalent diameter from SP2 to be mobility diameter. In addition, actual fresh BC
170 particles are not spheres and neither are some of the partially aged BC, but because
171 both the diameter measured from SP2 and the BC size distribution from the literatures
172 are with assumption of the particles being spheres, the fresh and aged BC in this study
173 are thereby assumed to be spherical particles.

174 **3 Theory**

175 3.1 Calculation of CCN concentration using κ -Köhler theory

176 In this study, we used the critical or cutoff particle diameter (D_{cut}) and particle
177 number size distribution to calculate N_{CCN} . The method to derive D_{cut} is based on
178 κ -Köhler theory (Petters and Kreidenweis, 2007), with the water vapor saturation ratio
179 over the aqueous solution droplet S given by:

$$180 \quad S = \frac{D^3 - D_p^3}{D^3 - D_p^3(1 - \kappa)} \exp\left(\frac{4\sigma_w M_w}{RT\rho_w D}\right), \quad (1)$$

181 where D is the droplet diameter, D_p is the dry diameter of the particle, M_w is the
182 molecular weight of water, σ_w is the surface tension of pure water, ρ_w is the density of
183 water, R is the gas constant, and T is the absolute temperature. When $\kappa > 0.1$ it can be
184 approximately expressed as:

$$185 \quad \kappa = \frac{4A^3}{27D_p^3 \ln^2 S_c}, \quad (2)$$

$$186 \quad A = \frac{4\sigma_w M_w}{RT\rho_w}, \quad (3)$$

187 where S_c is the particle critical supersaturation. The other variables in the equations
188 are: $T = 298.15$ K, $R = 8.315$ J K⁻¹ mol⁻¹, $\rho_w = 997.1$ kg m⁻³, $M_w = 0.018015$ kg mol⁻¹,
189 and $\sigma_w = 0.072$ J m⁻² (Rose et al., 2008).

190 For internally-mixed particles, κ is calculated as follows (Petters and
191 Kreidenweis, 2007; Gunthe et al., 2009):

192
$$\kappa_{chem} = \sum_i \varepsilon_i \kappa_i, \quad (4)$$

193
$$\kappa_{org} = f_{POA} \cdot \kappa_{POA} + f_{SOA} \cdot \kappa_{SOA}, \quad (5)$$

194 where κ_i and ε_i are the hygroscopicity parameter and volume fraction for the
 195 individual components in the mixture, and f_{POA} and f_{SOA} are the primary organic
 196 aerosol (POA) and secondary organic aerosol (SOA) mass fractions in the mixture.
 197 The Aerosol Mass Spectrometer (AMS) mainly measured the particle mass size
 198 distributions of SO_4^{2-} , NO_3^- , NH_4^+ and organic compounds, while the
 199 Zdanovskii-Stokes-Robinson relation requires the volume fractions of the particle
 200 chemical composition (Stokes and Robinson, 1966; Zdanovskii, 1948). A simplified
 201 ion pairing scheme is used to calculate the mass concentrations of the inorganic salts,
 202 which includes only NH_4NO_3 and $(\text{NH}_4)_2\text{SO}_4$ as possible salts (Gysel et al., 2007). In
 203 this study, we considered five components: NH_4NO_3 , $(\text{NH}_4)_2\text{SO}_4$, SOA, POA, and BC.
 204 The $\kappa_{(\text{NH}_4\text{NO}_3)}$ is equal to 0.67 and $\kappa_{(\text{NH}_4)_2\text{SO}_4}$ is equal to 0.61 (Petters and Kreidenweis,
 205 2007; Gunthe et al., 2009). The κ_{org} is estimated using the linear function derived by
 206 Mei et al. (2013a), namely, $\kappa_{org} = 2.10f_{44} - 0.11$, where f_{44} is dependent upon organics
 207 oxidation level. The mean κ_{org} is 0.10 in our case. The organics are classified into two
 208 factors: POA representing non-hygroscopic particles ($\kappa = 0$) and SOA representing
 209 hygroscopic species. In our study, the average contributions of POA and SOA to total
 210 organics were 0.53 and 0.47, respectively. On the basis of equation (5), $\kappa_{(\text{SOA})}$ is
 211 assumed to be 0.2. Also, $\kappa_{(\text{BC})}$ is assumed to be 0.

212 **3.2 Assumptions about mixing state and chemical composition**

213 To examine the influence of the mixing state and chemical composition on
214 CCN activation, five assumptions (Fig. 1) are used to predict N_{CCN} . Although the
215 assumption of completely internal or external mixing for ambient aerosols represents
216 two extremely simplified schemes and may be atmospherically unrealistic, it allows
217 us to understand the importance of the particle mixing state for predicting N_{CCN} . In
218 addition, size independent and dependent compositions are derived from the mass
219 concentrations of different species measured by the AMS so that the impact of
220 chemical composition on CCN activity can be examined. A detailed introduction of
221 the five assumption schemes follows.

222 **Assumption 1: internal mixture with bulk chemical composition (INT-BK)**

223 In this scheme, submicron particles are assumed to be internally mixed with bulk
224 chemical composition, where the mass fraction of each component (e.g. NH_4NO_3 ,
225 $(NH_4)_2SO_4$, SOA, POA, and BC) is uniform throughout the full size range as shown in
226 Fig. 1a. The overall κ is calculated from the bulk chemical composition measured by
227 the AMS based on the simple mixing rule (Equation 4) to obtain the critical diameter
228 at a given SS. For calculating N_{CCN} all (and only) particles with diameters greater than
229 D_{cut} are considered CCN-active. The total N_{CCN} is then calculated from the step-wise
230 integration of the PNSD for $D_p > D_{cut}$. The equations used in the calculations are as
231 follows,

232
$$CCN_{pre} = \int_{D_{cut}}^{D_{end}} n(\log D_p) d \log D_p \quad (6)$$

233
$$D_{cut} = \sqrt[3]{\frac{4A^3}{27 \sum_i \varepsilon_i \kappa_i \ln^2 S_c}} \quad (7)$$

234 where D_{cut} is the critical diameter, D_{end} is the upper size limit of the PNSD, $n(\log D_p)$
 235 is the function of the aerosol number size distribution, i is the chemical component
 236 element, and the other parameters are the same as those presented in Equations (2), (3)
 237 and (4).

238 **Assumption 2: internal mixture with size-resolved chemical composition**

239 **(INT-SR)**

240 For this scheme submicron particles are assumed to be internally mixed and the
 241 chemical composition is size-dependent as shown in Fig. 1d. The fractional
 242 contributions of the components at each size bin are derived from mass size
 243 distributions of the five species considered, i.e., NH_4NO_3 , $(\text{NH}_4)_2\text{SO}_4$, SOA, POA,
 244 and BC.

245 For this assumption, the critical diameter is derived from the total hygroscopic
 246 parameter, κ , at each size bin, j . For each size bin for which $D_{p,j}$ is $>$ than the
 247 calculated $D_{cut,j}$ the activated fraction was assumed to be 1.0 and for all others it was
 248 0.0. The N_{CCN} is calculated as follows:

$$CCN_{pre} = \int_{D_{begin}}^{D_{end}} n(\log D_p) d \log D_p \quad (8)$$

$$D_{cut,j} = \sqrt[3]{\frac{4A^3}{27 \sum_i \varepsilon_{ij} \kappa_{ij} \ln^2 S_c}} \quad (9)$$

where D_{begin} and D_{end} are the first and last diameters of the PNSD, $n(\log D_p)$ is the function of the aerosol number size distribution, i is the chemical component element, j is the PNSD size bin, and the other parameters are the same as those presented in Equations (2), (3) and (4).

Assumption 3: external mixture with bulk chemical composition (EXT-BK)

For this scheme the submicron aerosol is treated as an external mixture. This means that there are five types of particles, i.e., NH_4NO_3 , $(\text{NH}_4)_2\text{SO}_4$, SOA, POA, and BC, and each particle consists of a single component. The volume fraction of each component, which is derived from bulk mass concentrations, does not vary with size (as shown in Fig. 1b).

At a given S , the critical diameter of each particle type is retrieved from the κ of each component. The N_{CCN} of each aerosol type is calculated as the CCN-active particle number concentration multiplied by the bulk volume fraction of the components as expressed in Equation (10). The N_{CCN} of the five particle types are finally summed to obtain the total N_{CCN} . The specific equations are as follows,

$$266 \quad CCN_{pre} = \sum_i \left(\int_{D_{icut}}^{D_{end}} n(\log D_p) d \log D_p * V_i \right) \quad (10)$$

$$267 \quad D_{cut,i} = \sqrt[3]{\frac{4A^3}{27\kappa_i \ln^2 S_c}} \quad (11)$$

268 where $D_{cut,i}$ is calculated for each component, i , at a given SS, V_i is the volume
 269 fraction of each aerosol type, $n(\log D_p)$ is the function of the aerosol number size
 270 distribution, i is the chemical component element, and the other parameters are the
 271 same as those presented in Equations (2), (3) and (4).

272 **Assumption 4: external mixture with size-resolved chemical composition**

273 **(EXT-SR)**

274 As with the EXT-BK scheme the same five particle types are considered and
 275 their relative concentrations selected to match the measured composition. But unlike
 276 with the EXT-BK scheme the relative concentrations of the five particle types vary
 277 with particle size to capture the size-dependence of the measured composition, as is
 278 depicted in Fig. 1e. The volume fraction of each particle type at each size is first
 279 multiplied by the total particle number size distribution (PNSD) to get the $PNSD_i$ of
 280 each aerosol type. The N_{CCN} of each particle type is then obtained from the step-wise
 281 integration of the $PNSD_i$ for $D_p > D_{cut,i}$, and then summed to get the total N_{CCN} , as
 282 described by Equation (12). Similar to EXT-BK, the critical diameter of each particle
 283 type is also derived from the κ of each pure component at a given S.

$$CCN_{pre} = \sum_i \left(\int_{D_{begin}}^{D_{end}} (n(\log D_p) * V_{ij}) d \log D_p \right) \quad (12)$$

$$D_{cut,i} = \sqrt[3]{\frac{4A^3}{27\kappa_i \ln^2 S_c}} \quad (13)$$

where V_i is the volume fraction of each particle type in a size bin, $n(\log D_p)$ is the function of the aerosol number size distribution, i is the chemical component element, j is the particle size bin, and the other parameters are the same as those presented in Equations (2), (3) and (4).

Assumption 5: sulfate, nitrate, SOA and aged BC internally mixed, and POA and fresh BC externally mixed, and all components with size-resolved chemical composition (EI-SR)

At each particle size sulfate, nitrate, and SOA with BC-aged are treated as internally mixed, but POA and BC-fresh are present in separate particles and are non-hygroscopic. As with INT-SR and EXT-SR the chemical composition is size-dependent, as shown in Fig. 1c. The EI-SR scheme likely represents a case that is most similar to that of actual atmospheric aerosols in locations such as Beijing. The fresh and aged BC size distributions are determined from the total BC size distribution measured by the SP2 (Wu et al., 2017) and from the dependence of the fraction of internally mixed soot (F_{in}) on particle diameter (D_p) observed in urban Beijing by Cheng et al. (2012).

In this assumption the fresh BC and POA particles can serve as CCN only if their

303 diameter is larger than 200 nm; otherwise they are CCN-inactive. Thus, the total N_{CCN}
 304 of those externally mixed components (N_{CCN_EXT}) is calculated from the step-wise
 305 integration of the product of the PNSD and the volume fraction of the fresh BC and
 306 POA in each size bin larger than 200 nm.

307 The N_{CCN} of the remaining components (sulfate, nitrate, and SOA with BC-aged)
 308 that are treated as an internal mixture, denoted as N_{CCN_INT} , is predicted in the same
 309 way as for the INT-SR scheme, with the only difference being that the PNSD is first
 310 multiplied by the volume fraction of the mixed component particles for each size bin.
 311 The total N_{CCN} is thus calculated as the sum of N_{CCN_EXT} and N_{CCN_INT} . The
 312 specific equations are as follows,

$$313 \quad CCN_{pre} = \int_{D_{begin}}^{D_{200}} (n(\log D_p) * r_j) d \log D_p + \int_{D_{200}}^{D_{end}} n(\log D_p) d \log D_p \quad (14)$$

$$314 \quad D_{cut,j} = \sqrt[3]{\frac{4A^3}{27 \sum_i \varepsilon_{ij} \kappa_{ij} \ln^2 S_c}} \quad (15)$$

315 where D_{begin} and D_{end} are the first and last diameters of the PNSD, $n(\log D_p)$ is the
 316 function of the aerosol number size distribution, r is the volume fraction of the
 317 internal (hygroscopic) mixture at each size, i is the chemical component element, j is
 318 the particle size bin, and the other parameters are the same as those presented in
 319 Equations (2), (3) and (4).

320 **4 Results and discussion**

321 **4.1 Diurnal variations in aerosol properties**

322 Diurnal variations in mean PNSD and bulk chemical composition under
323 polluted and background conditions are shown in Fig. 2. Significant diurnal variations
324 in PNSD are observed during the campaign. For both polluted and background cases
325 the abrupt increases in concentration of small particles ($D_p < 100$ nm) from
326 1700–2000 local time (LT) are likely related to fresh primary emissions from cooking
327 and traffic sources (Wang et al., 2017; Zhao et al., 2017), which is also evident in the
328 significant increase in mass concentration of non-hygroscopic POA (Fig. 2d and 2e).
329 The peak amplitude in the PNSD that occurs from about 0800 to 1200 LT is probably
330 associated with secondary formation processes, which is indicated by an apparent
331 increase of nitrate, SOA and f_{44} (oxidation level of organics) in the morning (0800 LT)
332 when photochemistry becomes significant. The effect is more apparent on clean days.
333 In addition, the PNSD amplitude and BC and POA concentrations are high at
334 nighttime, suggesting an influence from the diurnal variation of the planetary
335 boundary layer (PBL) height. In particular, on polluted days the PBL plays a key role
336 in regulating the diurnal variation of primary components like POA and BC (e.g.,
337 Dzepina et al., 2009; Cross et al., 2009). On clean days secondary formation and
338 primary sources play dominant roles in regulating diurnal variations. The PNSD in
339 clean cases has peaks at smaller D_p (~30–40 nm, Fig. 1c) compared to polluted cases
340 (~100 nm), which is associated with particle growth accompanying atmospheric
341 chemistry processes during haze evolution (Guo et al., 2014; Wang et al., 2016).

342 **4.2 Cumulative Gaussian distribution function fit and parameters derived from**
343 **the CCN efficiency**

344 The activated fractions measured at the five supersaturation levels were fitted
345 using the following two functions (Rose et al., 2008; Mei et al., 2013b):

$$346 \quad R_a(S) = \frac{E}{2} \cdot (1 + \operatorname{erf}(\frac{\ln S - \ln S^*}{\sqrt{2}\sigma_s})), \quad (16)$$

$$347 \quad f_{N_{CCN}/N_{CN}} = a(1 + \operatorname{erf}(\frac{D - D_a}{\sigma_a\sqrt{2}})), \quad (17)$$

348 where $R_a(S)$ and $f_{(N_{CCN}/N_{CN})}$ are the CCN activation fractions, the maximum activation
349 fraction (MAF) is equal to E or $2a$, S^* and D_a are the midpoint activation
350 supersaturation and diameter, respectively, and σ_s and σ_a are the cumulative
351 distribution function (CDF) standard deviations. During this field campaign, 2580
352 size-resolved CCN efficiency spectra at five SS levels were measured. To illustrate
353 the characteristics of the activation spectra, the CDF fits are shown in Fig. 3 and in
354 Tables S1-2. A gradual increase in size-resolved AR with SS suggests that particles
355 had different hygroscopicities even at the same diameter. The heterogeneity of particle
356 chemical composition can be represented by the ratio of σ_a and D_a (i.e., σ_a/D_a), where
357 σ_a is the standard deviation derived from the cumulative Gaussian distribution
358 function (Eqn. 12) and D_a is the activation diameter (Rose et al., 2010). The ratio of
359 σ_a/D_a during the three periods is shown in Fig. 3b.

360 **4.2.1 CCN activation curves and heterogeneity of chemical components**

361 For larger particles with $D_p > 100$ nm, no significant differences were observed
362 in the CCN efficiency spectra (Fig. 3a), suggesting a similar hygroscopicity during the
363 three periods. For particles with $D_p < 100$ nm, the CCN efficiency spectrum observed
364 during the evening rush hour period showed a much more gradual increase (with
365 smaller slopes) in size-resolved AR than that derived for the other two periods. This is
366 attributed to the strong influence of POA emissions, which consist of less hygroscopic
367 and externally-mixed smaller particles mainly from cooking and traffic during the
368 evening rush hour period (also indicated by the increased σ_a/D_a). Particles with $D_p <$
369 100 nm emitted during the evening rush hour period require a higher SS to reach the
370 same AR. However, for $D_p > 100$ nm the slope of AR with respect to SS was steep
371 and near the instrumental limit obtained for a pure ammonium sulfate aerosol. [Che et](#)
372 [al. \(2016\)](#) have reported that particles larger than about 150 nm have relatively
373 uniform composition. This suggests that particles become more internally mixed with
374 growth from the Aitken mode to the accumulation mode. This feature is also
375 suggested by the decreasing σ_a/D_a with increasing particle diameter.

376 **4.2.2 Mean critical activation diameter**

377 The critical activation diameter at different SS levels under background and
378 polluted conditions is shown in Fig. 4. The difference in critical diameter between
379 polluted and background cases are calculated as $D_{p_POL} - D_{p_BG}$. At lower SS levels,

380 the critical diameters for polluted cases were slightly smaller than those observed on
381 clean days, suggesting larger particles are more CCN-active on polluted days. This is
382 expected based on HTDMA measurements that showed that particles in the
383 accumulation mode on polluted days are more hygroscopic than those on clean days
384 in urban Beijing (Wang et al., 2017). At higher SS the critical diameter on polluted
385 days was a little higher than that obtained under clean conditions, suggesting that
386 particles with D_p of ~40 nm are less CCN active. This is likely because a high
387 concentration of small and hygroscopic particles in the Aitken mode arise from the
388 photochemistry-driven nucleation process on clean days. However, in polluted cases,
389 small particles are mostly composed of hydrophobic POA from cooking and traffic
390 sources. This was also observed by Wang et al., (2017) who showed that 40 nm
391 particles are less hygroscopic on polluted days. However, the differences in critical
392 diameter between polluted and background cases are small, reflecting a relatively
393 minor influence of hygroscopicity on CCN activity.

394 **4.2.3 MAF**

395 As shown in Fig. 5, the maximum activated fractions on clean and polluted days
396 during the campaign are less than 1, which suggests that at least some sampled
397 aerosols were externally mixed (Gunthe et al., 2011). For example, the MAF for
398 particles with D_p of ~180 nm was around 0.78 at SS = 0.12% under background
399 conditions, indicating that ~22% of the particles are non-hygroscopic. The higher
400 MAFs under polluted conditions suggest a more internally mixed aerosol (Wu et al.,

401 2016; Wang et al., 2017). The MAF during the 1200–1400 LT period was highest,
402 which is likely due to strong photochemical aging processes that lead to more internal
403 mixing of the aerosol.

404 **4.3 CCN closure study and the sensitivity of predicted N_{CCN} to assumed aerosol** 405 **mixing state and chemical composition**

406 Fig. 6 shows the comparisons between predicted and measured N_{CCN} at different
407 SS levels under background and polluted conditions. The ratios of
408 predicted-to-measured N_{CCN} ($R_{CCN_p/m}$) ranged from 0.66 to 1.16, suggesting
409 significant influences of the different assumptions on CCN prediction. The EI-SR
410 assumption scheme predicts N_{CCN} very well, with $R_{CCN_p/m}$ of 0.90–0.98
411 (corresponding to a slight underestimation of 2-10%). For the EI-SR scheme,
412 hydrophobic POA and a portion of the BC are assumed to be externally mixed while
413 the other species (sulfate, nitrate, SOA and aged BC) are assumed to be internal
414 mixtures. The assumption is physically sound, and the result just implies that the
415 EI-SR represents well the actual mixing state and compositions of the particles. The
416 slight underestimation may due to an overestimation of fresh BC caused by the
417 method (see Section 3.1) that we used to retrieve it. Also, a slightly larger
418 underestimation of N_{CCN} for BG case in EI-SR scheme showed in Figure 6 may
419 suggest that aerosols during clean periods are mostly aged and internal-mixed.

420 The INT-SR and INT-BK schemes that assume the aerosol is internally mixed also
421 predict N_{CCN} reasonably well at lower SS. The prediction is better on background days,

422 reflecting the more homogenous aerosol composition in clean conditions. With
423 increasing SS this overestimation became more pronounced, which is likely due to
424 limitations of the AMS measurements. The AMS distributions show that the mass
425 concentration was most impacted by particles with diameters near ~100–400 nm.
426 Because particles in that size range tended to be more hygroscopic than those with
427 diameters < 100 nm, this leads to an overestimation of κ (underestimation of the
428 critical diameter) and a resulting overestimation of N_{CCN} at high SS. With decreasing
429 SS the critical diameter increased and the deviation using the INT-BK and INT-SR
430 schemes decreased. Detailed explanations about this effect have been given by [Wang](#)
431 [et al. \(2010\)](#) and [Zhang et al. \(2017\)](#). Overall, the INT-BK and INT-SR schemes
432 achieve CCN closure within what is deemed here an acceptable overprediction of
433 0-16%. The EXT-BK and EXT-SR schemes underestimated N_{CCN} , with $R_{CCN_p/m}$ of
434 0.66-0.75.

435 Overall, the internal-mixing schemes achieve much better closure than do those
436 assuming external mixtures. Our results suggest that freshly-emitted particles in
437 urban Beijing may experience a quick conversion and mixing with pre-existing
438 secondary particles, e.g. converting from externally mixed to internally mixed (or
439 from hydrophobic to hydrophilic, along with a decrease in the volume of POA and BC)
440 as reported previously ([Riemer et al., 2004](#); [Aggarwal and Kawamura, 2009](#); [Jimenez](#)
441 [et al., 2009](#); [Wu et al., 2016](#); [Peng et al., 2016](#)). In summary, under background
442 conditions, the INT-BK scheme achieved the best CCN closure, implying that the
443 INT-BK assumption is likely sufficient to predict CCN in clean continental regions.

444 However, in polluted regions, the EI-SR and INT-SR schemes may achieve better
445 closure.

446 As mentioned in Section 2.2, because the SP2 measures BC core diameter and
447 not the diameter of the BC-containing particle, the method would overestimate the BC
448 mass concentration of smaller particles but underestimate that of the larger ones. This
449 effect adds uncertainty to the CCN prediction when using the EXT-SR scheme and is
450 evaluated here (Fig. 7). For the evaluation, we predict N_{CCN} with the retrieved fresh
451 BC size distribution only in the EXT-SR scheme, which represents an upper limit of
452 the overestimation of the fresh BC size distribution due to the SP2 measurement.
453 Therefore, the result represents the largest underestimation of N_{CCN} caused by the
454 BC-containing particle effect. Our result shows that the underestimation of N_{CCN} is
455 reduced from 28% to 25% by changing the total BC size distribution to that of just the
456 fresh BC. That means that the overestimation of fresh BC due to the BC-containing
457 particle effect in the SP2 measurements would lead to a maximum underestimation of
458 3% of N_{CCN} . The minimal uncertainty contributed by uncertainty in the BC size
459 distribution could be explained by the small fractional contribution of BC to the total
460 particle concentration. In conclusion, such an effect is quite small or negligible
461 compared to the overall large underestimation of N_{CCN} with the EXT-SR assumption.

462 **4.4 Performance of the five schemes at different times of the day**

463 To investigate the performance of the five schemes at different times of the day,
464 the diurnal variations in the $R_{CCN_p/m}$ ($SS = 0.23\%$) derived by the schemes are shown

465 in Fig. 8. In general, the INT-BK, INT-SR, and EI-SR schemes can predict N_{CCN}
466 well during all periods of the day under polluted or background conditions. $R_{CCN_p/m}$
467 values are within the acceptable $\pm 20\%$ uncertainty range (Wang et al., 2010; Zhang
468 et al., 2017). Compared with other periods, the predicted N_{CCN} during the morning
469 and evening rush hour periods showed the most sensitivity to the different assumption
470 schemes, especially on clean days (Fig. 8b). For example, the $R_{CCN_p/m}$ derived using
471 the INT-SR schemes reaches values up to >1.2 , and the $R_{CCN_p/m}$ obtained using the
472 EXT-BK scheme decreased to a minimum value of ~ 0.5 . The INT-SR, INT-BK and
473 EI-SR assumptions overestimate N_{CCN} for the evening rush hour period by up to
474 $\sim 20\%$. This may be because most freshly emitted POA and BC particles during
475 evening traffic hours are hydrophobic and do not contribute to the N_{CCN} . In addition,
476 for EIS assumption, a portion of BC is assumed aged and internally-mixed with
477 sulfate, nitrate and SOA, as may reduce the actual fraction of fresh BC during rush
478 hour period and thereby lead to an overestimation of N_{CCN} .

479 Use of the EXT-BK or EXT-SR assumption for the polluted case resulted in a
480 predicted N_{CCN} that was underestimated by $\sim 30\text{-}40\%$ at night (0000–0600 LT).
481 Expectedly, the prediction using the two schemes improved during the daytime and
482 evening rush hours, e.g., the $R_{CCN_p/m}$ changed from about 0.6 to 0.8. This is likely
483 associated with heavy urban traffic emissions/residential cooking sources during the
484 daytime that lead to more externally-mixed particles under polluted conditions; while,
485 at night, the particles are less influenced by those local primary sources (Zhao. et al.,
486 2017). Wang et al. (2017) showed that the probability density function of κ during

487 rush hour has a bimodal distribution and a hydrophobic mode from locally-emitted
488 particles. This also leads to reasonably accurate estimates of N_{CCN} during nighttime
489 with larger error during the daytime when using the internal mixing assumptions
490 (INT-BK, INT-SR and EI-SR) for polluted cases (Fig. 8).

491 **4.5 Impact of mixing state and organic volume fraction on predicted N_{CCN} and** 492 **their variation with aerosol aging**

493 To further examine the sensitivity of predicted N_{CCN} to the particle mixing state
494 and organic volume fraction with the aging of organic particles, the relative deviation
495 between N_{CCN} predicted assuming internal and external mixtures as a function of κ_{org}
496 was calculated, with the results shown in Fig. 9. The schemes that assume internal and
497 external mixtures use bulk composition of organics, sulfate, and nitrate, which
498 simplifies the analysis and interpretation of the results. For the data collected
499 throughout the field campaign, the organic volume fraction is categorized as <50%,
500 50-60%, and >60%. The deviation between the concentrations predicted assuming
501 internal and external mixtures is calculated as $[(N_{CCN,INT-BK} - N_{CCN,EXT-BK})$
502 $(N_{CCN,EXT-BK})^{-1}]$. The result shows that the relative deviation increased as the
503 organic volume fraction increased. For organic volume fractions less than 50% the
504 maximum difference can only reach up to 20% (SS=0.76%). This is consistent with
505 previous studies that reported differences less than 20% when $x_{org} < 30\%$
506 (Sotiropoulou et al., 2006; Wang et al., 2010). The maximum deviation approaches to
507 100% for x_{org} of >60% at SS = 0.76%. Overall, the deviation is largest when the

508 organics are less or non-hygroscopic, i.e., when $\kappa_{\text{org}} < 0.05$. The deviation decreased
509 rapidly as κ_{org} increased to 0.05 in all cases. For κ_{org} of 0.1 the differences were less
510 than 20%, even with high organic fractions. Moreover, differences were 10% or less
511 for κ_{org} of 0.15, suggesting that the mixing state plays a minor role when κ_{org} exceeds
512 0.1.

513 **5 Conclusions**

514 In this study, we have investigated the importance of aerosol chemical
515 composition and mixing state on CCN activity based on measurements made during a
516 field campaign carried out in Beijing in the winter of 2016. The N_{CCN} was predicted
517 by applying κ -Köhler theory and using five schemes that assume different mixing
518 state and chemical composition combinations.

519 We show that there is a significant impact of the different assumptions on CCN
520 prediction, with $R_{\text{CCN}_{\text{p/m}}}$ ranging from 0.66 to 1.16. The best estimates of N_{CCN} under
521 both background and polluted conditions were obtained when using the EI-SR scheme,
522 with a resulting $R_{\text{CCN}_{\text{p/m}}}$ of 0.90–0.98. Under background conditions, the INT-BK
523 scheme also provided reasonable estimates, with $R_{\text{CCN}_{\text{p/m}}}$ ranging from 1.00–1.16.
524 This suggests that the INT-BK assumption is likely sufficient to predict CCN in clean
525 continental regions. On polluted days, the EI-SR and INT-SR schemes are believed to
526 achieve better closure than the INT-BK scheme due to the heterogeneity in particle
527 composition across different sizes. The improved closure obtained using the EI-SR
528 and INT-SR assumptions highlights the importance of knowing the size-resolved

529 chemical composition for CCN prediction in polluted regions. The EXT-SR and
530 EXT-BK schemes markedly underestimate N_{CCN} on both polluted and clean days,
531 with an $R_{CCN_p/m}$ of 0.66–0.75. The diurnal variations in $R_{CCN_p/m}$ show that the
532 predicted N_{CCN} during the evening rush hour period is most sensitive to the mixing
533 state assumptions. The $R_{CCN_p/m}$ ranged from ~ 0.5 to ~ 1.2 , reflecting the impact from
534 evening traffic and cooking sources (both with large amounts of hydrophobic POA).
535 But we also find that the particle mixing state plays a minor role when κ_{org} exceeds
536 0.1, even with a high organic fraction.

537 **Acknowledgements.** This work was funded by the NSFC research project (41675141
538 and 91544217), the fundamental Research Funds for the Central Universities, the
539 National Basic Research Program of China ‘973’ (2013CB955800), the NSCF-TAMU
540 Collaborative Research Grant Program (4141101031), and the Natural Science
541 Foundation (NSF) (AGS1534670). We thank all participants of the field campaign for
542 their tireless work and cooperation.

543

544 **References**

- 545 Aggarwal, S. G., and Kawamura, K.: Carbonaceous and inorganic composition in long-range
546 transported aerosols over northern Japan: Implication for aging of water-soluble organic
547 fraction, *Atmos. Environ.*, 43, 2532–2540, doi:10.1016/j.atmosenv.2009.02.032, 2009.
- 548 Albrecht, B. A.: Aerosols, cloud microphysics, and fractional cloudiness, *Science*, 245, 1227–1230,
549 1989.
- 550 Andreae, M. O., and Rosenfeld, D.: Aerosol–cloud–precipitation interactions. Part 1. The nature
551 and sources of cloud-active aerosols, *Earth-Science Reviews*, 89, 13–41,
552 doi:10.1016/j.earscirev.2008.03.001, 2008.
- 553 Aiken, A. C., Salcedo, D., Cubison, M. J., Huffman, J. A., DeCarlo, P. F., Ulbrich, I. M.,
554 Docherty, K. S., Sueper, D., Kimmel, J. R., Worsnop, D. R., Trimborn, A., Northway, M.,
555 Stone, E. A., Schauer, J. J., Volkamer, R. M., Fortner, E., de Foy, B., Wang, J., Laskin, A.,
556 Shutthanandan, V., Zheng, J., Zhang, R., Gaffney, J., Marley, N. A., Paredes-Miranda, G.,
557 Arnott, W. P., Molina, L. T., Sosa, G., and Jimenez, J. L.: Mexico City aerosol analysis
558 during MILAGRO using high resolution aerosol mass spectrometry at the urban supersite
559 (T0) - Part 1: Fine particle composition and organic source apportionment, *Atmos. Chem.*
560 *Phys.*, 9, 6633– 6653, doi:10.5194/acp-9-6633-2009, 2009.
- 561 Bhattu, D., and Tripathi, S. N.: CCN closure study: Effects of aerosol chemical composition and
562 mixing state, *J. Geophys. Res. Atmos.*, 120, 766–783, doi:10.1002/2014jd021978, 2015.
- 563 Broekhuizen, K., Chang, R. Y. W., Leaitch, W. R., Li, S. M., and Abbatt, J. P. D.: Closure between
564 measured and modeled cloud condensation nuclei (CCN) using size-resolved aerosol
565 compositions in downtown Toronto, *Atmos. Chem. Phys.*, 6, 2513–2524,
566 10.5194/acp-6-2513-2006, 2006.
- 567 Chang, R. Y. W., Liu, P. S. K., Leaitch, W. R., and Abbatt, J. P. D.: Comparison between measured
568 and predicted CCN concentrations at Egbert, Ontario: Focus on the organic aerosol fraction at a
569 semirural site, *Atmos. Environ.*, 41, 8172–8182, 2007.
- 570 Charlson, R. J., Schwartz, S. E., Hales, J. M., Cess, R. D., Coakley, J. A., Jr., Hansen, J. E., and
571 Hofmann, D. J.: Climate forcing by anthropogenic aerosols, *Science*, 255, 423+, 1992.
- 572 Che, H. C., Zhang, X. Y., Wang, Y. Q., Zhang, L., Shen, X. J., Zhang, Y. M., Ma, Q. L., Sun, J. Y.,
573 Zhang, Y. W., and Wang, T. T.: Characterization and parameterization of aerosol cloud
574 condensation nuclei activation under different pollution conditions, *Sci. Rep.*, 6,
575 doi:10.1038/srep24497, 2016.

576 Cross, E. S., Onasch, T. B., Canagaratna, M., Jayne, J. T., Kimmel, J., Yu, X. Y., Alexander, M. L.,
577 Worsnop, D. R., and Davidovits, P.: Single particle characterization using a light scattering
578 module coupled to a time of flight aerosol mass spectrometer, *Atmos. Chem. Phys.*, 9,
579 7769–7793, doi:10.5194/acp-9-7769-2009, 2009.

580 Cheng, Y. F., Su, H., Rose, D., Gunthe, S. S., Berghof, M., Wehner, B., Achtert, P., Nowak, A.,
581 Takegawa, N., Kondo, Y., Shiraiwa, M., Gong, Y. G., Shao, M., Hu, M., Zhu, T., Zhang, Y. H.,
582 Carmichael, G. R., Wiedensohler, A., Andreae, M. O., and Pöschl, U.: Size-resolved
583 measurement of the mixing state of soot in the megacity Beijing, China: diurnal cycle, aging
584 and parameterization, *Atmospheric Chemistry and Physics*, 12, 4477–4491,
585 10.5194/acp-12-4477-2012, 2012.

586 Dall'Osto, M., Harrison, R. M., Coe, H., Williams, P. I., and Allan, J. D.: Real time chemical
587 characterization of local and regional nitrate aerosols, *Atmos. Chem. Phys.*, 9, 3709–3720,
588 10.5194/acp-9-3709-2009, 2009.

589 DeCarlo, P. F., Kimmel, J. R., Trimborn, A., et al.: Field-deployable, high-resolution,
590 time-of-flight aerosol mass spectrometer, *Anal. Chem.*, 78, 8281–8289, 2006.

591 Deng, Z. Z., Zhao, C. S., Ma, N., Ran, L., Zhou, G. Q., Lu, D. R., and Zhou, X. J.: An examination
592 of parameterizations for the CCN number concentration based on in situ measurements of
593 aerosol activation properties in the North China Plain, *Atmos. Chem. Phys.*, 13, 6227–6237,
594 10.5194/acp-13-6227-2013, 2013.

595 Dusek, U., Frank, G. P., Hildebrandt, L., et al.: Size matters more than chemistry for cloud
596 nucleating ability of aerosol particles, *Science*, 312, 1375–1378, 2006.

597 Dzepina, K., Volkamer, R. M., Madronich, S., Tulet, P., Ulbrich, I. M., Zhang, Q., Cappa, C. D.,
598 Ziemann, P. J., and Jimenez, J. L.: Evaluation of recently proposed secondary organic aerosol
599 models for a case study in Mexico City, *Atmos. Chem. Phys.*, 9, 5681–5709,
600 doi:10.5194/acp-9-5681-2009, 2009.

601 Ervens, B., Cubison, M., Andrews, E., et al.: Prediction of cloud condensation nucleus number
602 concentration using measurements of aerosol size distributions and composition and light
603 scattering enhancement due to humidity, *J. Geophys. Res. Atmos.*, 112, D10S32,
604 doi:10.1029/2006JD007426, 2007.

605 Gunthe, S. S., King, S. M., Rose, D., Chen, Q., Roldin, P., Farmer, D. K., Jimenez, J. L., Artaxo, P.,
606 Andreae, M. O., Martin, S. T., and Pöschl, U.: Cloud condensation nuclei in pristine tropical
607 rainforest air of Amazonia: size resolved measurements and modeling of atmospheric aerosol
608 composition and CCN activity, *Atmos. Chem. Phys.*, 9, 7551–7575,
609 doi:10.5194/acp-9-7551-2009, 2009.

610 Gunthe, S. S., Rose, D., Su, H., Garland, R. M., Achtert, P., Nowak, A., Wiedensohler, A., Kuwata,
611 M., Takegawa, N., Kondo, Y., Hu, M., Shao, M., Zhu, T., Andreae, M. O., and Pöschl, U.: Cloud
612 condensation nuclei (CCN) from fresh and aged air pollution in the megacity region of Beijing,
613 *Atmos. Chem. Phys.*, 11, 11023–11039, doi:10.5194/acp-11-11023-2011, 2011.

614 Guo, S., Hu, M., Zamora, M. L., Peng, J., Shang, D., Zheng, J., Du, Z., Wu, Z., Shao, M., Zeng, L.,
615 Molina, M. J., and Zhang, R.: Elucidating severe urban haze formation in China, *P. Natl. Acad.*
616 *Sci. USA*, 111, 17373–17378, doi:10.1073/pnas.1419604111, 2014.

617 Gysel, M., Crosier, J., Topping, D. O., Whitehead, J. D., Bower, K. N., Cubison, M. J., Williams, P.
618 I., Flynn, M. J., McFiggans, G. B., and Coe, H.: Closure study between chemical composition
619 and hygroscopic growth of aerosol particles during TORCH2, *Atmos. Chem. Phys.*, 7,
620 6131–6144, doi:10.5194/acp-7-6131-2007, 2007.

621 Jimenez, J. L., Canagaratna, M. R., et al.: Evolution of organic aerosols in the atmosphere,
622 *Science*, 326, 1525–1529, 2009.

623 Kawana, K., Nakayama, T., and Mochida, M.: Hygroscopicity and CCN activity of atmospheric
624 aerosol particles and their relation to organics: Characteristics of urban aerosols in Nagoya,
625 Japan, *J. Geophys. Res. Atmos.*, 121, 4100–4121, doi:10.1002/2015jd023213, 2016.

626 Lance, S., Medina, J., Smith, J., and Nenes, A.: Mapping the operation of the DMT continuous
627 flow CCN counter, *Aerosol Sci. Technol.*, 40, 242–254, 2006.

628 Li, Y., Zhang, F., Li, Z., Sun, L., Wang, Z., Li, P., Sun, Y., Ren, J., Wang, Y., Cribb, M., and Yuan,
629 C.: Influences of aerosol physiochemical properties and new particle formation on CCN activity
630 from observation at a suburban site of China, *Atmos. Res.*, 188, 80–89,
631 doi:10.1016/j.atmosres.2017.01.009, 2017.

632 Li, Z., F. Niu, J. Fan, Y. Liu, D. Rosenfeld, and Y. Ding.: The long-term impacts of aerosols on the
633 vertical development of clouds and precipitation, *Nature Geosci.* 4, doi: 10.1038/NGEO1313,
634 2011.

635 Liu, H. J., Zhao, C. S., Nekat, B., Ma, N., Wiedensohler, A., van Pinxteren, D., Spindler, G.,
636 Müller, K., and Herrmann, H.: Aerosol hygroscopicity derived from size-segregated chemical
637 composition and its parameterization in the North China Plain, *Atmos. Chem. Phys.*, 14,
638 2525–2539, doi:10.5194/acp-14-2525-2014, 2014.

639 Ma, Y., Brooks, S. D., Vidaurre, G., Khalizov, A. F., Wang, L., and Zhang, R.: Rapid modification
640 of cloud-nucleating ability of aerosols by biogenic emissions, *Geophys. Res. Lett.*, 40(23),
641 6293–6297, 2013.

642 McFiggans, G., Artaxo, P., Baltensperger, U., Coe, H., Facchini, M. C., Feingold, G., Fuzzi, S.,
643 Gysel, M., Laaksonen, A., Lohmann, U., Mentel, T. F., Murphy, D. M., O'Dowd, C. D., Snider,
644 J. R., and Weingartner, E.: The effect of physical and chemical aerosol properties on warm
645 cloud droplet activation, *Atmos. Chem. Phys.*, 6, 2593–2649, doi:10.5194/acp-6-2593-2006,
646 2006.

647 Medina, J., Nenes, A., Sotiropoulou, R. E. P., Cottrell, L. D., Ziemba, L. D., Beckman, P. J., and
648 Griffin, R. J.: Cloud condensation nuclei closure during the International Consortium for
649 Atmospheric Research on Transport and Transformation 2004 campaign: Effects of size
650 resolved composition, *J. Geophys. Res. Atmos.*, 112, D10S31, doi:10.1029/2006JD007588,
651 2007.

652 Mei, F., Setyan, A., Zhang, Q., and Wang, J.: CCN activity of organic aerosols observed
653 downwind of urban emissions during CARES, *Atmos. Chem. Phys.*, 13, 12155–12169,
654 doi:10.5194/acp-13-12155-2013, 2013a.

655 Mei, F., Hayes, P. L., Ortega, A. M., Taylor, J. W., Allan, J. D., Gilman, J. B., Kuster, W. C., de
656 Gouw, J. A., Jimenez, J. L., and Wang, J.: Droplet activation properties of organic aerosols
657 observed at an urban site during CalNex-LA, *J. Geophys. Res.*, 118, 2903-2917,
658 10.1002/jgrd.50285, 2013b.

659 Meng, J. W., Yeung, M. C., Li, Y. J., Lee, B. Y. L., and Chan, C. K.: Size-resolved cloud
660 condensation nuclei (CCN) activity and closure analysis at the HKUST Supersite in Hong Kong,
661 *Atmos. Chem. Phys.*, 14, 10267–10282, doi:10.5194/acp-14-10267-2014, 2014.

662 Moore, R. H., Nenes, A., and Medina, J.: Scanning mobility CCN analysis—A method for fast
663 measurements of size-resolved CCN distributions and activation kinetics, *Aerosol Sci. Technol.*,
664 44, 861–871, doi:10.1080/02786826.2010.498715, 2010.

665 Moore, R. H., Cerully, K., Bahreini, R., Brock, C. A., Middlebrook, A. M., and Nenes, A.:
666 Hygroscopicity and composition of California CCN during summer 2010, *J. Geophys. Res.*
667 *Atmos.*, 117, D00V12, doi:10.1029/2011JD017352, 2012.

668 Paatero, P., and U. Tapper (1994), Positive matrix factorization: A non-negative factormodel with
669 optimal utilization of error estimates of data values, *Environmetrics*, 5, 111–126.

670 Peng, J., Hu, M., Guo, S., Du, Z., Zheng, J., & Shang, D., et al. (2016). Markedly enhanced
671 absorption and direct radiative forcing of black carbon under polluted urban environments.
672 *Proceedings of the National Academy of Sciences of the United States of America*, 113(16),
673 4266.

674 Petters, M. D., and Kreidenweis, S. M.: A single parameter representation of hygroscopic growth

675 and cloud condensation nucleus activity, *Atmos. Chem. Phys.*, 7, 1961–1971,
676 doi:10.5194/acp-7-1961-2007, 2007.

677 Riemer, N., Vogel, H., and Vogel, B.: Soot aging time scales in polluted regions during day and
678 night, *Atmos. Chem. Phys.*, 4, 1885–1893, doi:10.5194/acp-4-1885-2004, 2004.

679 Rose, D., Gunthe, S. S., Mikhailov, E., Frank, G. P., Dusek, U., Andreae, M. O., and Pöschl, U.:
680 Calibration and measurement uncertainties of a continuous-flow cloud condensation nuclei
681 counter (DMT-CCNC): CCN activation of ammonium sulfate and sodium chloride aerosol
682 particles in theory and experiment, *Atmos. Chem. Phys.*, 8, 1153–1179,
683 doi:10.5194/acp-8-1153-2008, 2008.

684 Rose, D., Nowak, A., Achtert, P., Wiedensohler, A., Hu, M., Shao, M., Zhang, Y., Andreae, M. O.,
685 and Pöschl, U.: Cloud condensation nuclei in polluted air and biomass burning smoke near the
686 mega-city Guangzhou, China. Part 1: Size-resolved measurements and implications for the
687 modeling of aerosol particle hygroscopicity and CCN activity, *Atmos. Chem. Phys.*, 10,
688 3365–3383, doi:10.5194/acp-10-3365-2010, 2010.

689 Rosenfeld, D., Lohmann, U., Raga, G. B., O’Dowd, C. D., Kulmala, M., Fuzzi, S., Reissell, A.,
690 and Andreae, M. O.: Flood or drought: How do aerosols affect precipitation?, *Science*, 321,
691 doi:10.1126/science.1160606, 2008.

692 Sotiropoulou, R.-E. P., Medina, J., and Nenes, A.: CCN predictions: Is theory sufficient for
693 assessments of the indirect effect?, *Geophys. Res. Lett.*, 33, doi:10.1029/2005gl025148, 2006.

694 Stokes, R. H., and Robinson, R. A.: Interactions in aqueous nonelectrolyte solutions. I.
695 Solute-solvent equilibria, *J. Phys. Chem.*, 70, 2126–2130, 1966.

696 Sun, J., Zhang, Q., Canagaratna, M. R., Zhang, Y., Ng, N. L., Sun, Y., Jayne, J. T., Zhang, X.,
697 Zhang, X., and Worsnop, D. R.: Highly time- and size-resolved characterization of submicron
698 aerosol particles in Beijing using an Aerodyne Aerosol Mass Spectrometer, *Atmos. Environ.*, 44,
699 131–140, doi:10.1016/j.atmosenv.2009.03.020, 2010.

700 Sun, Y. L., Wang, Z. F., Fu, P. Q., Yang, T., Jiang, Q., Dong, H. B., Li, J., and Jia, J. J.: Aerosol
701 composition, sources and processes during wintertime in Beijing, China, *Atmos. Chem. Phys.*,
702 13, 4577–4592, doi:10.5194/acp-13-4577-2013, 2013.

703 Sun, Y. L., Wang, Z. F., Du, W., Zhang, Q., Wang, Q. Q., Fu, P. Q., Pan, X. L., Li, J., Jayne, J., and
704 Worsnop, D. R.: Long-term real-time measurements of aerosol particle composition in Beijing,
705 China: Seasonal variations, meteorological effects, and source analysis, *Atmos. Chem. Phys.*, 15,
706 10149–10165, doi:10.5194/acp-15-10149-2015, 2015.

707 Sun, Y., Chen, C., Zhang, Y., Xu, W., Zhou, L., Cheng, X., Zheng, H., Ji, D., Li, J., Tang, X., Fu, P.,
708 and Wang, Z.: Rapid formation and evolution of an extreme haze episode in Northern China
709 during winter 2015, *Sci. Rep.*, 6, doi:10.1038/srep27151, 2016.

710 Textor, C., Schulz, M., Guibert, S., Kinne, S., Balkanski, Y., Bauer, S., Berntsen, T., Berglen, T.,
711 Boucher, O., Chin, M., Dentener, F., Diehl, T., Easter, R., Feichter, H., Fillmore, D., Ghan, S.,
712 Ginoux, P., Gong, S., Grini, A., Hendricks, J., Horowitz, L., Huang, P., Isaksen, I., Iversen, I.,
713 Kloster, S., Koch, D., Kirkevåg, A., Kristjansson, J. E., Krol, M., Lauer, A., Lamarque, J. F., Liu,
714 X., Montanaro, V., Myhre, G., Penner, J., Pitari, G., Reddy, S., Seland, Ø., Stier, P., Takemura,
715 T., and Tie, X.: Analysis and quantification of the diversities of aerosol life cycles within
716 AeroCom, *Atmos. Chem. Phys.*, 6, 1777–1813, doi:10.5194/acp-6-1777-2006, 2006.

717 Twomey, S.: The influence of pollution on the shortwave albedo of clouds, *J. Atmos. Sci.*, 34,
718 1149–1152, doi:10.1175/1520-0469(1977)034(1149: TIOPOT)2.0.CO;2, 1977.

719 Wang, J., Flagan, R. C., and Seinfeld, J. H.: A differential mobility analyzer (DMA) system for
720 submicron aerosol measurements at ambient relative humidity, *Aerosol Sci. Technol.*, 37, 46–52,
721 2003.

722 Wang, J., Cubison, M. J., Aiken, A. C., Jimenez, J. L., and Collins, D. R.: The importance of
723 aerosol mixing state and size-resolved composition on CCN concentration and the variation of
724 the importance with atmospheric aging of aerosols, *Atmos. Chem. Phys.*, 10, 7267–7283,
725 doi:10.5194/acp-10-7267-2010, 2010.

726 Wang, G., Zhang, R., Gomez, M. E., Yang, L., Zamora, M. L., Hu, M., ... & Li, J. (2016).
727 Persistent sulfate formation from London Fog to Chinese haze. *Proceedings of the National*
728 *Academy of Sciences*, 113(48), 13630-13635.

729 Wang, Y., Zhang, F., Li, Z., Tan, H., Xu, H., Ren, J., Zhao, J., Du, W., and Sun, Y.: Enhanced
730 hydrophobicity and volatility of submicron aerosols under severe emission control conditions in
731 Beijing, *Atmos. Chem. Phys.*, 17, 5239–5251, doi:10.5194/acp-17-5239-2017, 2017.

732 Wiedensohler, A., Cheng, Y. F., Nowak, A., Wehner, B., Achtert, P., Berghof, M., Birmili, W., Wu,
733 Z. J., Hu, M., Zhu, T., Takegawa, N., Kita, K., Kondo, Y., Lou, S. R., Hofzumahaus, A., Holland,
734 F., Wahner, A., Gunthe, S. S., Rose, D., Su, H., and Pöschl, U.: Rapid aerosol particle growth
735 and increase of cloud condensation nucleus activity by secondary aerosol formation and
736 condensation: A case study for regional air pollution in northeastern China, *J. Geophys. Res.*
737 *Atmos.*, 114, D00G08, doi:10.1029/2008JD010884, 2009.

738 Wu, Y., Wang, X., Tao, J., Huang, R., Tian, P., Cao, J., Zhang, L., Ho, K.-F., Han, Z., and Zhang,
739 R.: Size distribution and source of black carbon aerosol in urban Beijing during winter haze
740 episodes, *Atmos. Chem. Phys.*, 17, 7965–7975, doi:10.5194/acp-17-7965-2017, 2017.

741 Wu, Z. J., Zheng, J., Shang, D. J., Du, Z. F., Wu, Y. S., Zeng, L. M., Wiedensohler, A., and Hu, M.:
742 Particle hygroscopicity and its link to chemical composition in the urban atmosphere of Beijing,
743 China, during summertime, *Atmos. Chem. Phys.*, 16, 1123–1138,
744 doi:10.5194/acp-16-1123-2016, 2016.

745 Yum, S. S., Hudson, J. G., Song, K. Y., and Choi, B. C.: Springtime cloud condensation nuclei
746 concentrations on the west coast of Korea, *Geophys. Res. Lett.*, 32, L09814,
747 doi:10.1029/2005GL022641, 2005.

748 Yum, S. S., Roberts, G., Kim, J. H., Song, K. Y., and Kim, D. Y.: Submicron aerosol size
749 distributions and cloud condensation nuclei concentrations measured at Gosan, Korea, during
750 the Atmospheric Brown Clouds East Asian Regional Experiment 2005, *J. Geophys. Res. Atmos.*,
751 112, D22S32, doi:10.1029/2006JD008212, 2007.

752 Zdanovskii, B.: Novyi Metod Rascheta Rastvorimostei Elektrolitovv Mnogokomponentnykh
753 Sistema, *Zh. Fiz. Khim+*, 22, 1478–1495, 1948.

754 Zhang, F., Li, Y., Li, Z., Sun, L., Li, R., Zhao, C., Wang, P., Sun, Y., Liu, X., Li, J., Li, P., Ren, G.,
755 and Fan, T.: Aerosol hygroscopicity and cloud condensation nuclei activity during the AC³Exp
756 campaign: Implications for cloud condensation nuclei parameterization, *Atmos. Chem. Phys.*,
757 14, 13423–13437, doi:10.5194/acp-14-13423-2014, 2014.

758 Zhang, F., Li, Z., Li, Y., Sun, Y., Wang, Z., Li, P., Sun, L., Wang, P., Cribb, M., Zhao, C., Fan, T.,
759 Yang, X., and Wang, Q.: Impacts of organic aerosols and its oxidation level on CCN activity
760 from measurement at a suburban site in China, *Atmos. Chem. Phys.*, 16, 5413–5425,
761 doi:10.5194/acp-16-5413-2016, 2016.

762 Zhang F., Wang Y., Peng J., Ren J., Zhang R., Sun Y., Don Collin., Yang X., Li Z.: Uncertainty
763 in predicting CCN activity of aged and primary aerosols. *Journal of Geophysical*
764 *Research: Atmospheres*. 10.1002/2017JD027058, 2017.

765 Zhang, Z., Engling, G., Lin, C.-Y., Chou, C. C. K., Lung, S.-C. C., Chang, S.-Y., Fan, S., Chan,
766 C.-Y., and Zhang, Y.-H.: Chemical speciation, transport and contribution of biomass burning
767 smoke to ambient aerosol in Guangzhou, a mega city of China, *Atmos. Environ.*, 44, 3187–3195,
768 doi:10.1016/j.atmosenv.2010.05.024, 2010.

769 Zhao, J., Du, W., Zhang, Y., Wang, Q., Chen, C., Xu, W., Han, T., Wang, Y., Fu, P., Wang, Z., Li,
770 Z., and Sun, Y.: Insights into aerosol chemistry during the 2015 China Victory Day parade:
771 results from simultaneous measurements at ground level and 260 m in Beijing, *Atmos. Chem.*
772 *Phys.*, 17, 3215–3232, doi:10.5194/acp-17-3215-2017, 2017.

773 Zheng, G. J., Duan, F. K., Su, H., Ma, Y. L., Cheng, Y., Zheng, B., Zhang, Q., Huang, T., Kimoto,

774 T., Chang, D., Pöschl, U., Cheng, Y. F., and He, K. B.: Exploring the severe winter haze in
775 Beijing: the impact of synoptic weather, regional transport and heterogeneous reactions, *Atmos.*
776 *Chem. Phys.*, 15, 2969–2983, doi:10.5194/acp-15-2969-2015, 2015.

777 Zhang, Q., Worsnop, D. R., Canagaratna, M. R., and Jimenez, J. L.: Hydrocarbon-like and
778 oxygenated organic aerosols in Pittsburgh: insights into sources and processes of organic
779 aerosols, *Atmos. Chem. Phys.*, 5, 3289–3311, doi:10.5194/acp-5-3289-2005, 2005.

780

781

782

783

784

785

786

787

788

789

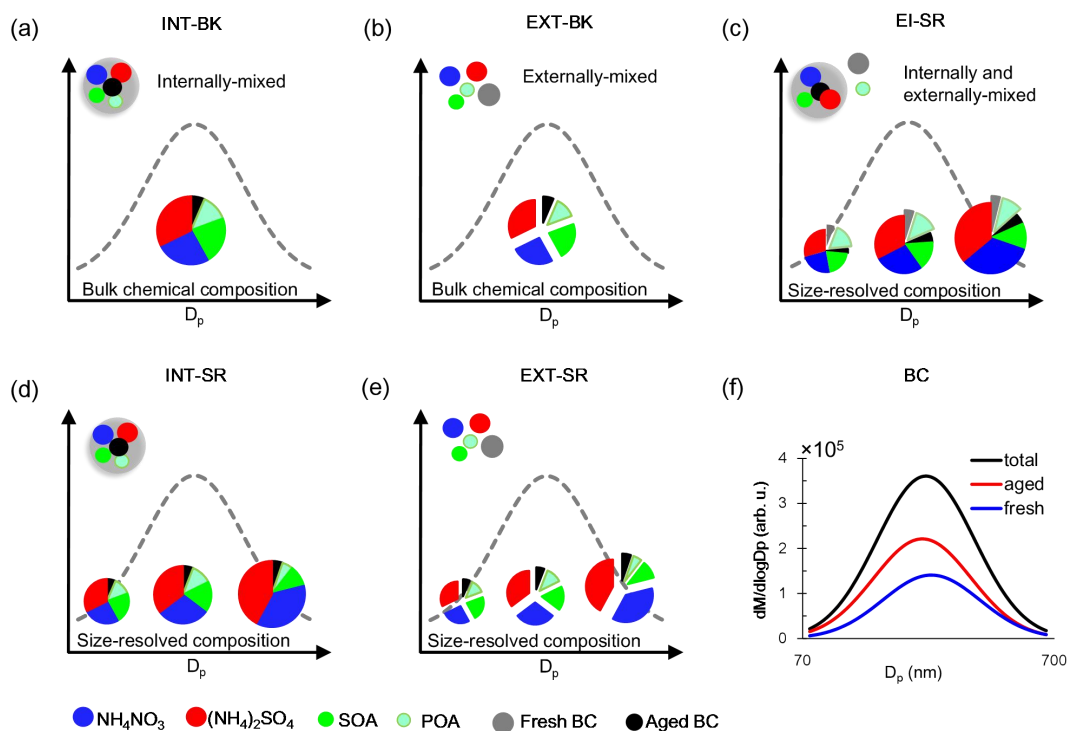
790

791

792

793

794



796

797 **Figure 1** Schematic representation of the five different schemes: (a) INT-BK, (b)

798 EXT-BK, (c) EI-SR, (d) INT-SR, and (e) EXT-SR. And the BC size distribution (f)

799 used in this study. The fresh and aged BC size distribution are retrieved from the total

800 BC size distribution measured by the SP2 (Wu et al., 2017) and the dependence of the

801 fraction of internally mixed soot (F_{in}) on particle diameter (D_p) observed in urban

802 Beijing (Cheng et al., 2012). The total BC size distribution is used in the INT-SR and

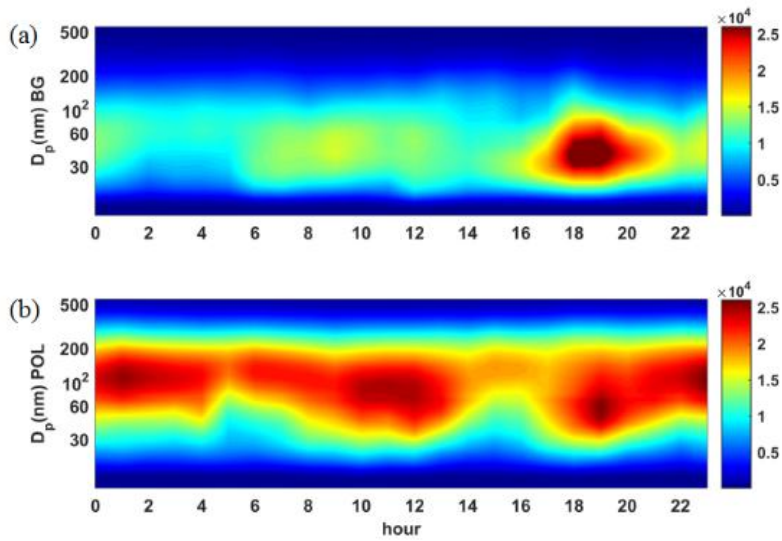
803 EXT-SR schemes, and the aged and fresh BC distributions are used in the EI-SR

804 scheme. In the EI-SR scheme, some BC particles are assumed to already be aged and

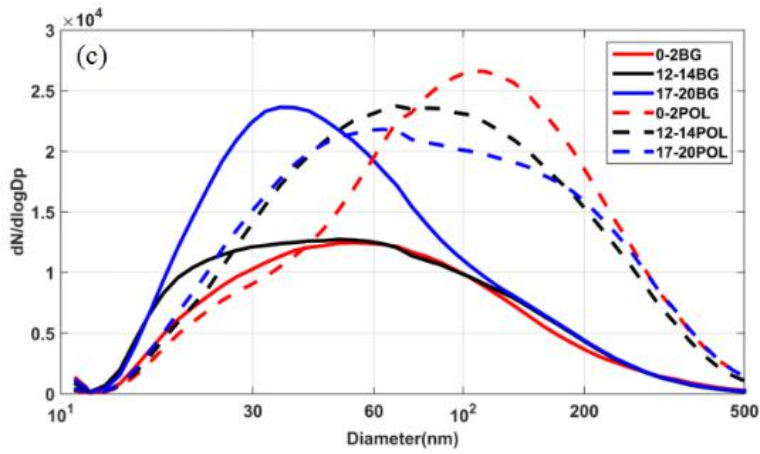
805 thus internally-mixed with sulfate, nitrate and SOA, and some of them together with

806 POA are freshly emitted and assumed not yet aged/coated by other species

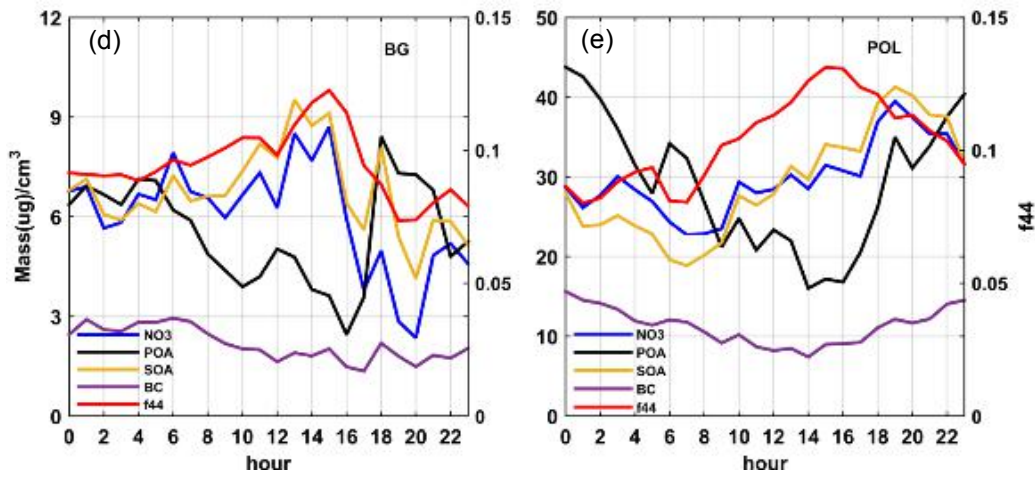
807 (externally-mixed).



808



809



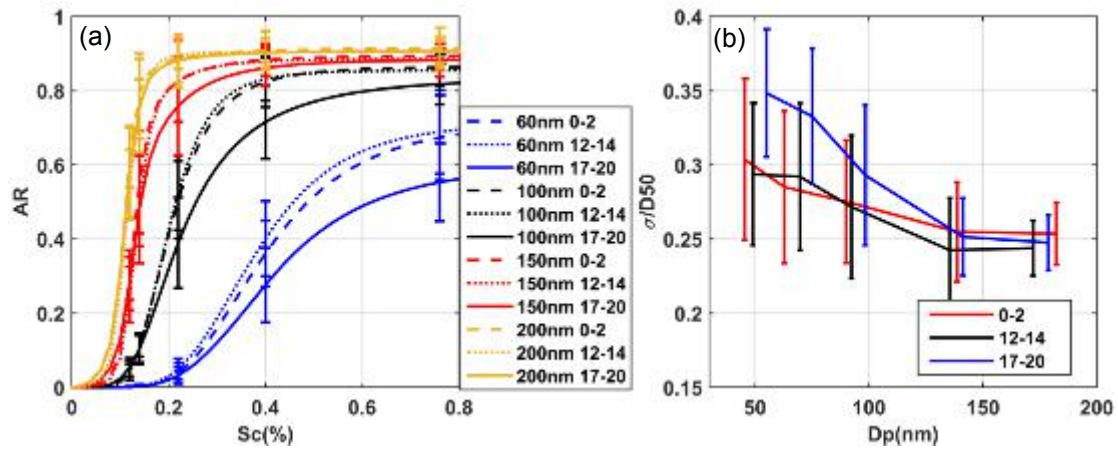
810

811 **Figure 2.** Diurnal variations in aerosol properties at the IAP site during the APHH

812 field experiment, including the particle number size distribution measured by the

813 SMPS under (a) background (BG) and (b) polluted (POL) conditions; (c) mean
814 particle number size distribution measured by the SMPS during three periods
815 (0000–0200 LT, 1200–1400 LT, and 1700–2000 LT) under BG and POL conditions;
816 bulk chemical component mass concentrations (NO_3 , POA, SOA, and BC) and f_{44}
817 made under (d) BG and (e) POL conditions.

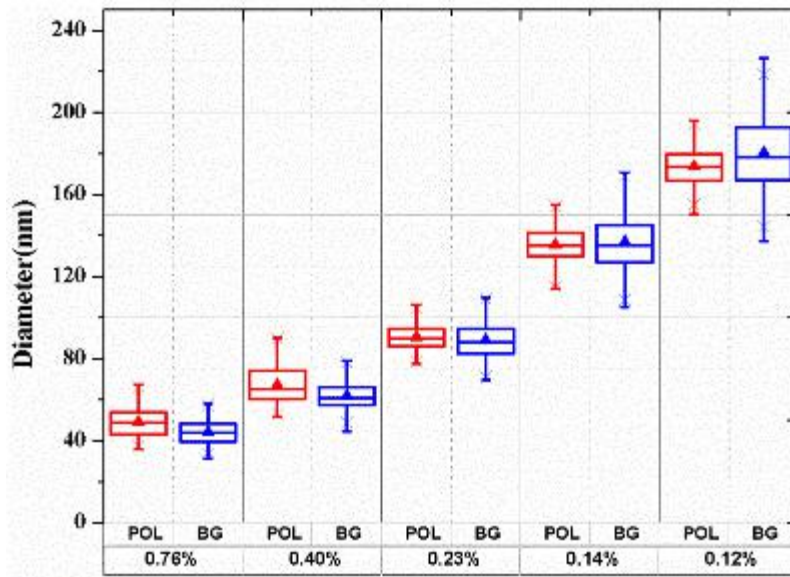
818



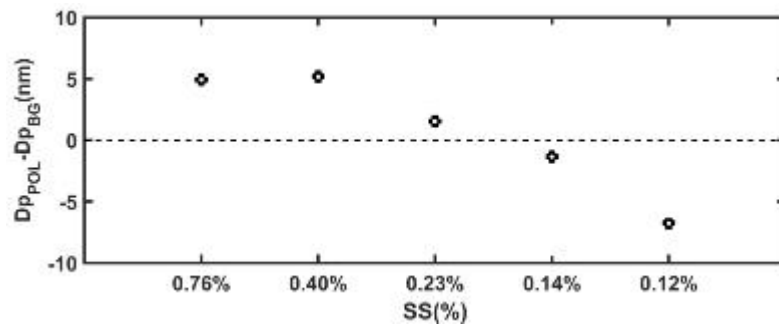
819

820 **Figure 3.** (a) Averaged fitted CCN efficiency spectra during the nighttime period
 821 (0000–0200 LT, dashed lines), the noontime period (1200–1400 LT, dotted lines) and
 822 the evening rush hour period (1700–2000 LT, solid lines) for different diameters (60,
 823 100, 150, and 200 nm); (b) the heterogeneity of aerosol particles (σ_a/D_a) derived from
 824 Equation (7) during the three selected periods.

825



826

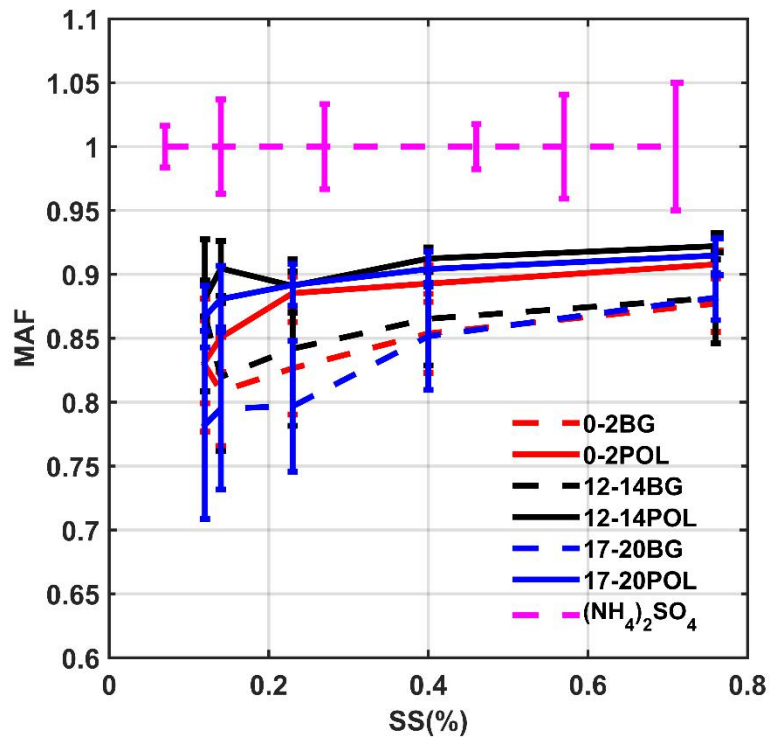


827

828 **Figure 4.** Top: Retrieved mean critical activation diameters at SS = 0.12, 0.14, 0.23,
 829 0.40, and 0.76% under background (BG) and polluted (POL) conditions. The box
 830 plots show mean critical activation diameters at the 25th, 50th, and 75th percentiles.
 831 Bottom: Difference in the mean critical activation diameter between BG and POL
 832 cases.

833

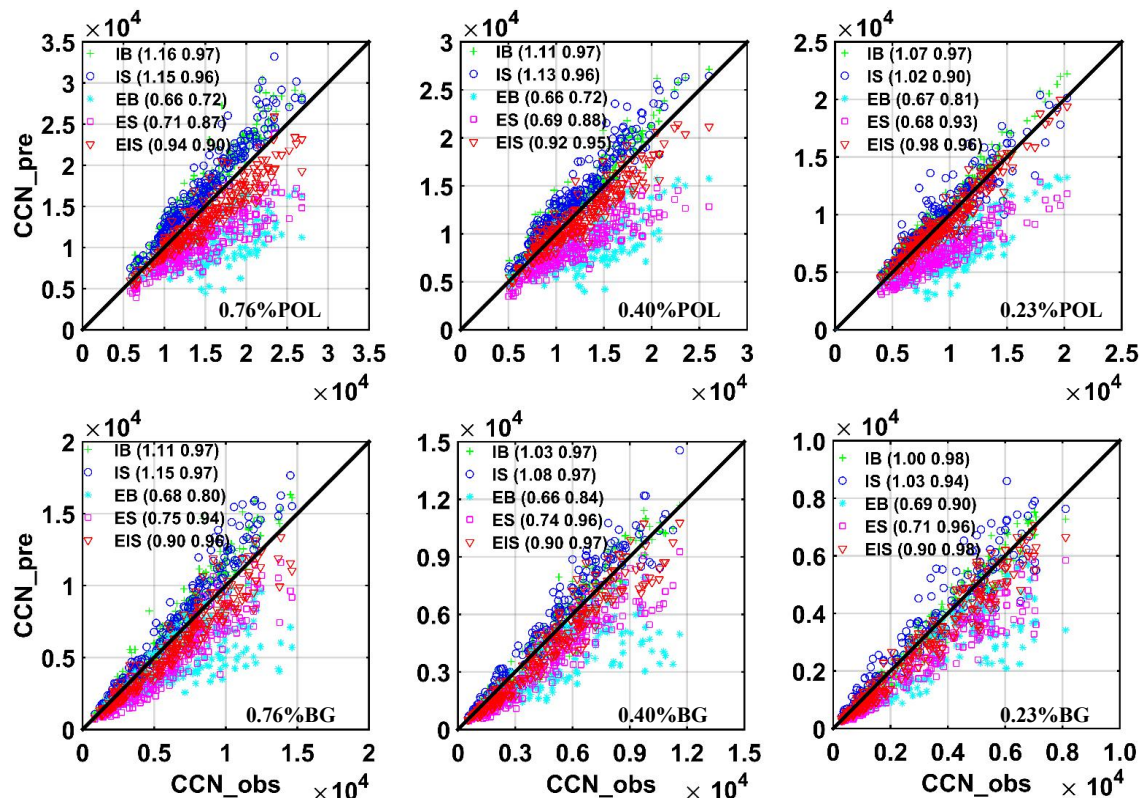
834



835

836 **Figure 5.** Mean maximum active fractions (MAFs) of CCN activation spectra under
 837 polluted (POL) and background (BG) conditions during the three periods, i.e.,
 838 0000–0200 LT, 1200–1400 LT, and 1700–2000 LT. The MAF of pure (NH₄)₂SO₄
 839 particles at the different SS levels (magenta line) is also plotted.

840



842

843 + INT-BK Internal mixture, bulk composition

844 o INT-SR Internal mixture, size-resolved composition

845 * EXT-BK External mixture, bulk composition

846 □ EXT-SR External mixture, size-resolved composition

847 ▽ EI-SR External mixture, POA and BC externally mixed, size-resolved composition

848 **Figure 6.** Predicted N_{CCN} as a function of measured N_{CCN} using the five assumptions

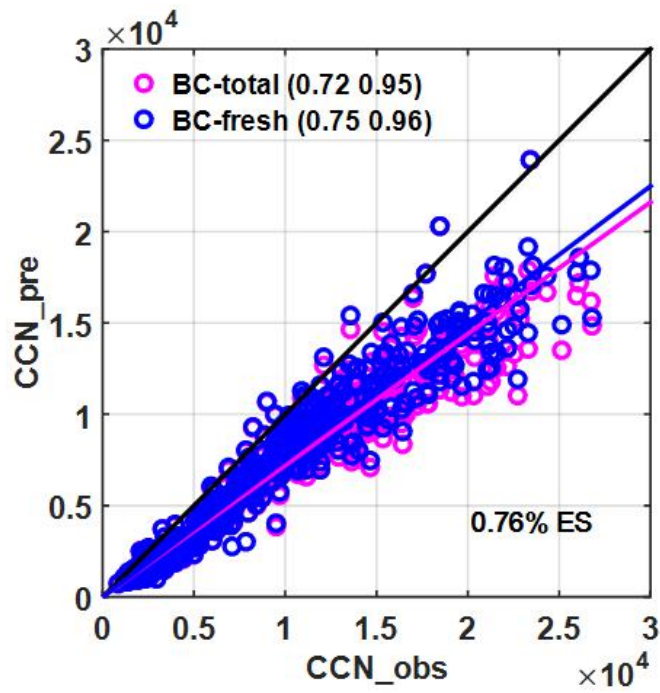
849 (colored symbols) at three supersaturation levels (0.23, 0.40, and 0.76%) under

850 polluted (POL) and background (BG) conditions. The numbers in parentheses are the

851 slope (first number) and the correlation coefficient (second number).

852

853



854

855 **Figure 7.** Predicted N_{CCN} as a function of measured N_{CCN} using the EXT-SR
 856 assumption (colored symbols) at $S=0.76\%$. The pink and blue circles denote the
 857 results predicted by using total and fresh BC size distributions, respectively. The
 858 numbers in parentheses are the slope (first number) and the correlation coefficient
 859 (second number).

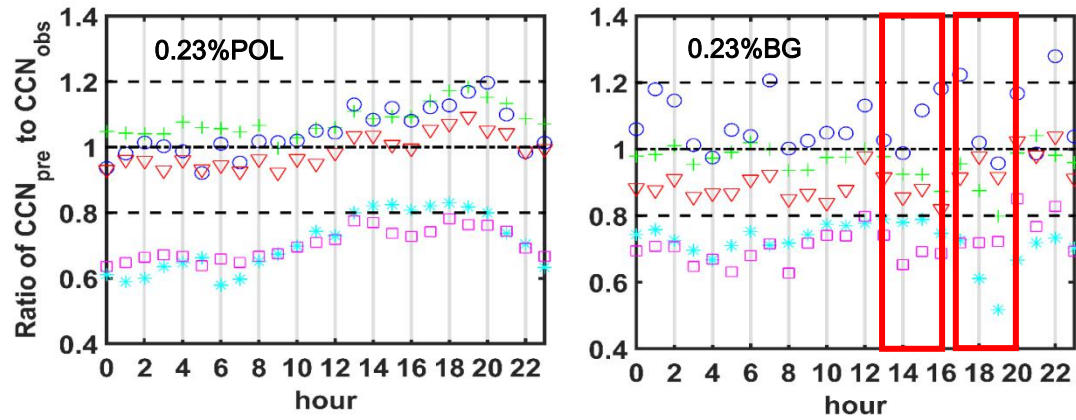
860

861

862

863

864



865

866 + INT-BK Internal mixture, bulk composition

867 o INT-SR Internal mixture, size-resolved composition

868 * EXT-BK External mixture, bulk composition

869 □ EXT-SR External mixture, size-resolved composition

870 ▽ EI-SR External mixture, POA and BC externally mixed, size-resolved composition

871 **Figure 8.** Diurnal variations in the ratio of predicted-to-measured N_{CCN} at a
 872 supersaturation level of 0.23% under background (BG) and polluted (POL)
 873 conditions.

874

875

876

877

878

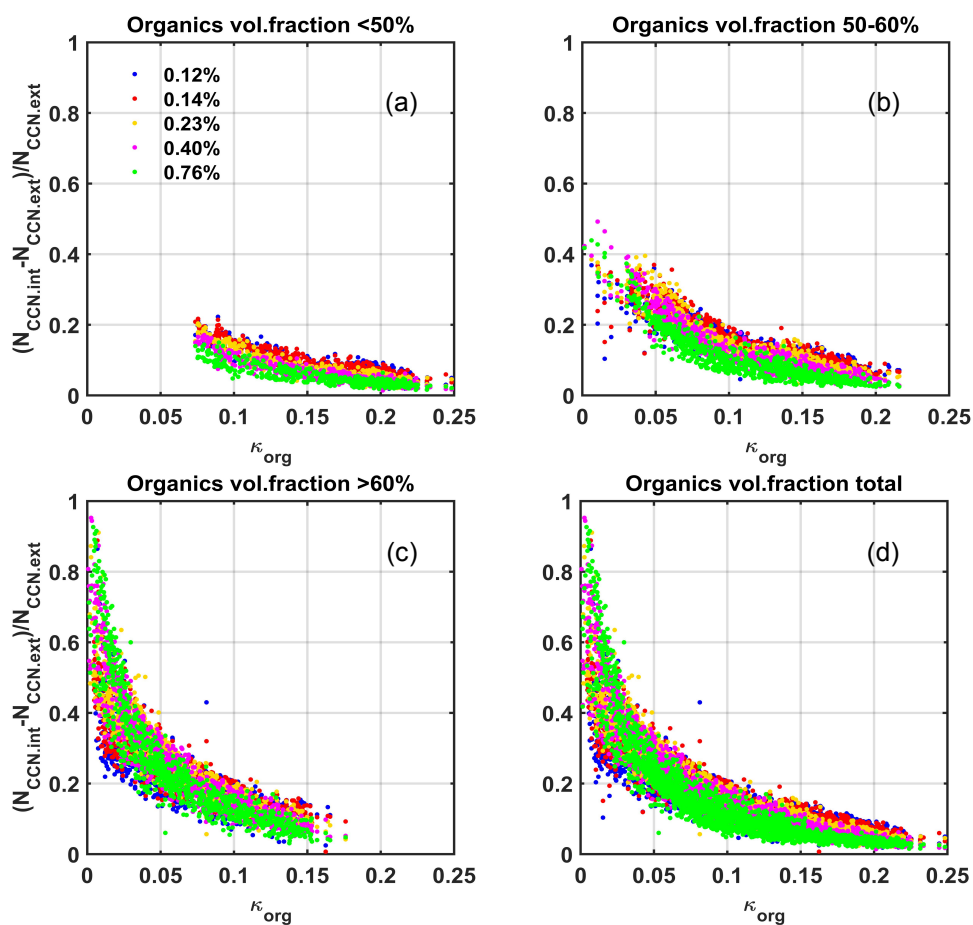
879

880

881

882

883



884

885

886

887

888

889

890

891

892

Figure 9. Relative deviations between N_{CCN} predicted under the assumptions of internal (INT-BK) and external (EXT-BK) mixtures $[(N_{CCN,INT-BK} - N_{CCN,EXT-BK}) / (N_{CCN,EXT-BK})^{-1}]$ as a function of κ_{org} when organic volume fractions of <50 (a), 50-60 (b), >60% (c) and all observed data points (d). The solid with different colors represent different supersaturation levels. The different colors denote the different organic fractions.